Numerical simulation of the flow over a hypersonic waverider using the method for splitting into physical processes

D S Yatsukhno

A.Ishlinsky Institute for Problems in Mechanics of the Russian academy of sciences, Vernadsky prospect 101(1), Moscow, 119526, Russia

E-mail: yatsukhno-ds@rambler.ru

Abstract. The aim of the study is to obtain hypersonic waverider aerodynamic characteristics over the angle-of-attack range from 0° to 10° at Mach 4. The simplified virtual model of the waverider was designed. The Navier-Stokes equations solution was performed using computer code into which the method for splitting into physical processes was implemented. The unstructured grid was used in the computational process.

1. Introduction

The hypersonic waveriders is a class of vehicles having the following performance advantages:

- The reusable space vehicles
- An ability to take off and land horizontally like conventional airplane
- High aerodynamic efficiency

The waverider shape is derived from the inviscid conical flow field and the shock wave shape. The upper surface is produced by the axisymmetric method of characteristics. The lower surface is generated by solutions of the Taylor-Maccoll differential equations [1] given as

$$\frac{\gamma-1}{2}\left(1-V_r^2-\left(\frac{dV_r}{d\theta}\right)^2\right)\left(2V_r+\cot(\theta)\frac{dV_r}{d\theta}+\frac{d^2V_r}{d\theta^2}\right)-\frac{dV_r}{d\theta}\left(V_r\frac{dV_r}{d\theta}+\frac{dV_r}{d\theta}\frac{d^2V_r}{d\theta^2}\right)=0 \qquad (1)$$

$$V_\theta=\frac{dV_r}{d\theta} \qquad (2)$$

Here γ – ratio of specific heats, θ – angle from the conical axis, V_r – radial velocity, V_θ – normal velocity. Shock wave shape and streamlines about cone are depicted in Figure 1. Waveriders have a performance advantage of maximization lift-to-drag ratio compared with other hypersonic vehicles. It is achieved due to a shock wave attached everywhere along the leading edge. A second feature of the waverider is that upper surface is oriented, so that it does not disturb the overcoming flow. The general waverider disadvantage is that the high lift-to-drag ratio can be realized for a specific operation condition with respect to flight altitude, Mach number and shock wave shape [2].

The viscous effects are not considered in the above mentioned family of vehicles designing. However, waveriders have a higher lift-to-drag ratio if viscous effects as well as transition from

laminar to turbulent flow are taken into consideration. This class of aircraft is named a viscous-optimized waveriders [3, 4]. Thus, waverider designing is a complex process including geometric modeling using methods of computational fluid dynamics (CFD) and optimization process.

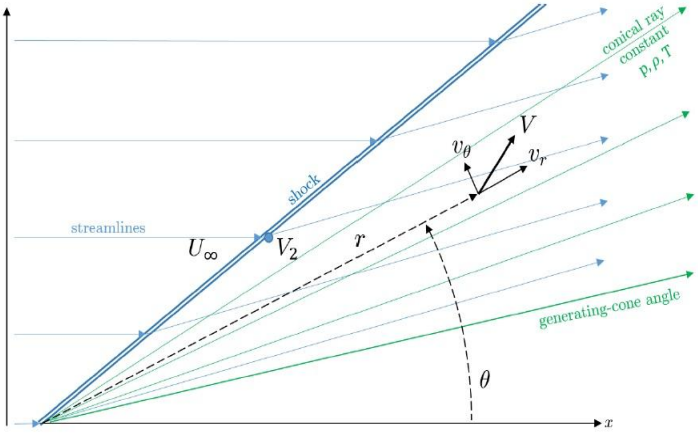

Figure 1. Taylor-Maccoll inviscid cone similarity solution [2].

2. Design of the virtual prototype

The waverider virtual model used for calculations in this study is shown in figure 2. This vehicle is based on viscous-optimized waverider [5] which was designed using Maryland Axisymmetric Waverider Program (MAXWARP) [3, 4]. The model background includes CFD predictions and experimental data obtained from tests in the Unitary Plan Wind Tunnel (UPWT) [6]. The main purpose of this work is to compare current numerical simulation results with mentioned data. It was performed with aid UST3D computer code which has already been validated [7, 8].

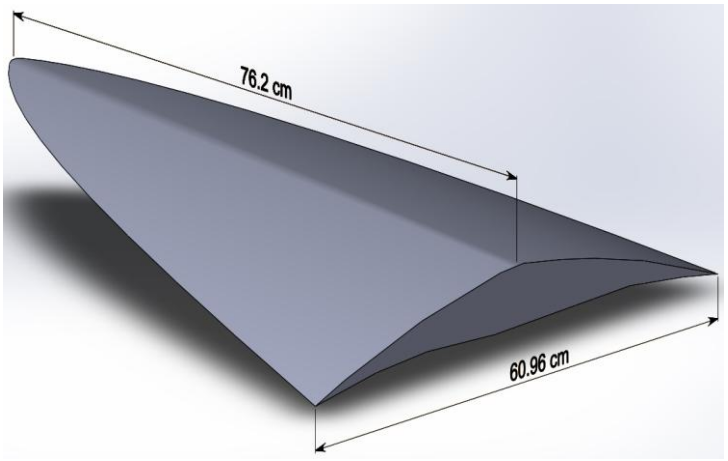

Figure 2. Waverider model designed for free-stream Mach number of 4.

The elements of the singular cone flow method were used for the mentioned waverider designing. The model has a sharp leading edge. The waverider is assumed to have optimal aerodynamic performance at the Reynolds number per foot of $2 \cdot 10^6$.

3. Mesh

The three-dimensional unstructured mesh was generated for the present computational study. It consists of 2262354 finite elements and 393370 nodes. A slip boundary condition is imposed

by 64094 fictive elements which were generated along the waverider surfaces. The mesh is shown in figure 3.

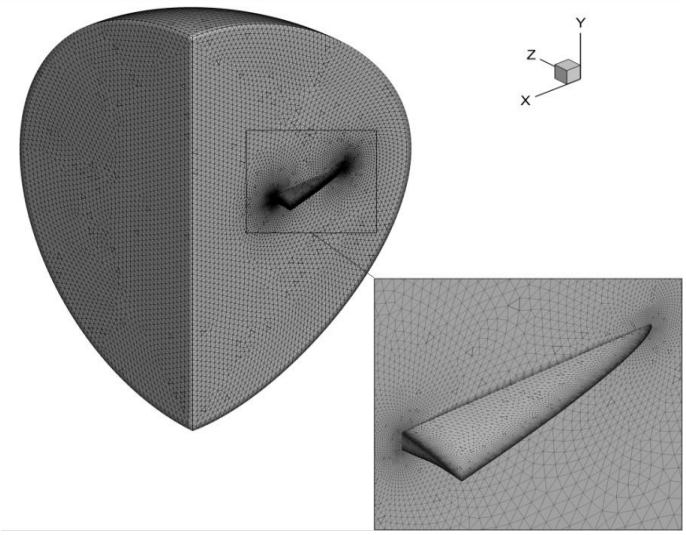

Figure 3. Waverider model mesh.

The most important unstructured mesh feature is the application of the finite volumes method elements [7]. The averaged values of the finite volume derivatives are determined in the framework of this approach. The Navier-Stokes equations are approximated by the following relations

$$\left\langle \frac{\partial f}{\partial \alpha} \right\rangle_{V_i} = \frac{1}{V_i}\int_{V_i} \frac{\partial f}{\partial \alpha} dV = \frac{1}{V_i}\int_{V_i} f\boldsymbol{i}\cdot d\boldsymbol{S} \approx \frac{1}{V_i}\sum_{j=1}^{4} S_i^j n_{i,j}^{\alpha} f_i^j \tag{3}$$

$$f = \left(u, \mathrm{v}, w, \mathrm{p}, \mathrm{q}_{\alpha}, \tau_{\alpha\beta}\right); i = 1...\mathrm{N}; \; j = 1...4; \alpha = x, y, z; \; \beta = x, y, z$$

Here u, v, w – components of the velocity vector; p – pressure; q_{α} – components of the heat flux vector; $\tau_{\alpha\beta}$ – components of the viscous stress tensor; V_i – i-element volume; S_i^j – i-element j-face surface area; $n_{i,j}^{\alpha}$ – i-element j-face normal component.

4. Numerical simulation

4.1. Problem formulation

The three-dimensional Navier-Stokes equations are used for perfect viscous compressible gas flow describing and presented in the vector form

$$\frac{\partial \mathbf{w}}{\partial t} + \frac{\partial \boldsymbol{F}^x(\mathbf{w})}{\partial x} + \frac{\partial \boldsymbol{F}^y(\mathbf{w})}{\partial y} + \frac{\partial \boldsymbol{F}^z(\mathbf{w})}{\partial z} = \frac{\partial \boldsymbol{G}^x(\mathbf{w})}{\partial x} + \frac{\partial \boldsymbol{G}^y(\mathbf{w})}{\partial y} + \frac{\partial \boldsymbol{G}^z(\mathbf{w})}{\partial z} \tag{4}$$

$$\mathbf{w} = \left(\rho, \rho u, \rho \mathrm{v}, \rho w, \rho E\right)^T$$

$$\boldsymbol{F}^x = \left(\rho u, \rho u^2 + p, \rho u \mathrm{v}, \rho u w, \rho u E + p u\right)^T$$

$$\boldsymbol{F}^y = \left(\rho \mathrm{v}, \rho u \mathrm{v}, \rho \mathrm{v}^2 + p, \rho \mathrm{v} w, \rho \mathrm{v} E + p \mathrm{v}\right)^T$$

$$\boldsymbol{F}^z = \left(\rho w, \rho u w, \rho \mathrm{v} w, \rho w^2 + p, \rho w E + p w\right)^T$$

$$\boldsymbol{G}^x = \left(0, \tau_{xx}, \tau_{yx}, \tau_{zx}, u\tau_{xx} + \nu\tau_{yx} + w\tau_{zx} - q_x\right)^T$$

$$\boldsymbol{G}^y = \left(0, \tau_{xy}, \tau_{yy}, \tau_{zy}, u\tau_{xy} + \nu\tau_{yy} + w\tau_{zy} - q_y\right)^T$$

$$\boldsymbol{G}^z = \left(0, \tau_{xz}, \tau_{yz}, \tau_{zz}, u\tau_{xz} + \nu\tau_{yz} + w\tau_{zz} - q_z\right)^T$$

In the above equations $\mathbf{w}$ – conservative variables vector; $\boldsymbol{F}^x, \boldsymbol{F}^y, \boldsymbol{F}^z$ – projections of the convective flow vector; $\boldsymbol{G}^x$, $\boldsymbol{G}^y$, $\boldsymbol{G}^z$ – projections of the viscous flow vector, ρ – density, E – specific total energy. The components of the viscous stress tensor are given as

$$\tau_{xx} = \mu\left(\frac{4}{3}\frac{\partial u}{\partial x} - \frac{2}{3}\frac{\partial \nu}{\partial y} - \frac{2}{3}\frac{\partial w}{\partial z}\right),\ \tau_{xy} = \tau_{yx} = \mu\left(\frac{\partial \nu}{\partial x} + \frac{\partial u}{\partial y}\right),$$

$$\tau_{yy} = \mu\left(\frac{4}{3}\frac{\partial \nu}{\partial y} - \frac{2}{3}\frac{\partial u}{\partial x} - \frac{2}{3}\frac{\partial w}{\partial z}\right),\ \tau_{yz} = \tau_{zy} = \mu\left(\frac{\partial w}{\partial y} + \frac{\partial \nu}{\partial z}\right), \quad (5)$$

$$\tau_{zz} = \mu\left(\frac{4}{3}\frac{\partial w}{\partial z} - \frac{2}{3}\frac{\partial u}{\partial x} - \frac{2}{3}\frac{\partial \nu}{\partial y}\right),\ \tau_{xz} = \tau_{zx} = \mu\left(\frac{\partial u}{\partial z} + \frac{\partial w}{\partial x}\right)$$

Here μ – dynamic viscosity. In addition to the Navier-Stokes equations the perfect gas state equation is considered

$$p = (\gamma - 1)\rho U = (\gamma - 1)\rho\left[E - 0.5\left(u^2 + \nu^2 + w^2\right)\right] \quad (6)$$

Here U – specific internal gas energy. The thermophysical parameters temperature dependence is not taken into account.

The solution method basis is the original unsteady Navier-Stokes system splitting into physical processes [8]. Each of the time steps calculation fall into three stages. First, the flow parameters reference values are determined without convective effects. The Euler equations are the result of the initial system simplification. Second, mass flows over the cell boundaries are considered. Accordingly, the effects of transition are calculated. And, finally, flow parameters are determined by laws of conservation. The mass, momentum and energy redistribution are accomplished at this stage.

4.2. Boundary conditions

The four types of the boundary conditions were used for the numerical simulation. The free-stream boundary conditions are imposed on the front boundary and are described as

$$\rho_{enter} = \rho_\infty$$

$$u_{enter} = u_\infty$$

$$\nu_{enter} = \nu_\infty \quad (7)$$

$$w_{enter} = w_\infty$$

$$E_{enter} = E_\infty = \frac{p_\infty}{(\gamma - 1)\rho_\infty} + \frac{u_\infty^2 + \nu_\infty^2 + w_\infty^2}{2}$$

Here $p_\infty, \rho_\infty, u_\infty, \nu_\infty, w_\infty, E_\infty$ – free-stream flow parameters (pressure, density, velocity vector components, specific total energy).

The open boundary conditions were implemented for the gas outflow from computational domain:

$$\left.\frac{\partial \rho}{\partial \boldsymbol{n}}\right|_{exit} = 0$$

$$\left.\frac{\partial u}{\partial \boldsymbol{n}}\right|_{exit} = \left.\frac{\partial \nabla}{\partial \boldsymbol{n}}\right|_{exit} = \left.\frac{\partial w}{\partial \boldsymbol{n}}\right|_{exit} = 0 \tag{8}$$

$$\left.\frac{\partial E}{\partial \boldsymbol{n}}\right|_{exit} = 0$$

Here $\boldsymbol{n}$ – specific normal vector.

The impermeability boundary conditions were applied in the Euler equations solution process on the solid wall. The normal velocity is equal to zero. The tangent velocity behavior is characterized as continuous. It is described by no-slip boundary conditions:

$$\left.\frac{\partial p}{\partial \boldsymbol{n}}\right|_{wall} = 0 \tag{9}$$

$$u^n\Big|_{wall} = \nabla^n\Big|_{wall} = w^n\Big|_{wall} = 0$$

The insulated wall boundary condition was realized for the energy equation:

$$\left.\frac{\partial T}{\partial \boldsymbol{n}}\right|_{wall} = 0 \tag{10}$$

The Navier-Stokes equations describe viscous gas model on the wall by a slip boundary conditions. The insulated wall boundary condition was used for the energy equation:

$$\left.\frac{\partial p}{\partial \boldsymbol{n}}\right|_{wall} = 0$$

$$u^n\Big|_{wall} = \nabla^n\Big|_{wall} = w^n\Big|_{wall} = 0 \tag{11}$$

$$\left.\frac{\partial T}{\partial \boldsymbol{n}}\right|_{wall} = 0$$

The fixed temperature is supported on the body surface:

$$T\big|_{wall} = T_{wall} \tag{12}$$

The symmetry boundary conditions are realized in the symmetry plane. It is the same as the inviscid boundary conditions on the insulated wall:

$$\left.\frac{\partial p}{\partial \boldsymbol{n}}\right|_{symm} = 0$$

$$u^n\Big|_{symm} = \nabla^n\Big|_{symm} = w^n\Big|_{symm} = 0 \tag{13}$$

$$\left.\frac{\partial T}{\partial \boldsymbol{n}}\right|_{symm} = 0$$

5. Results

The numerical simulation results are presented in figures 5 – 8. The comparison between CFD predictions, experimental data and computational study results was performed at Mach 4 and various angles of attack assuming that base pressure equal to free-stream pressure. The obtained aerodynamic characteristics have the similar type of behavior as experimental data. The lift and drag coefficients increase as angle of attack increases. The reasonable accordance between experimental data and solutions was obtained for the angle-of-attack range from 0° to 4°. The calculation error increases at angles of attack above 4°.

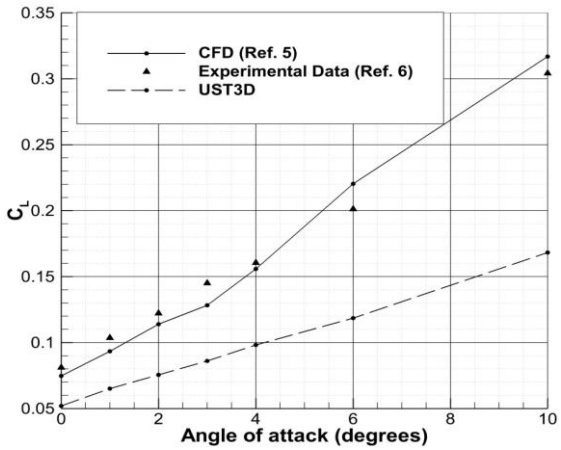

Figure 5. Lift coefficient values for different angles of attack at Mach 4.

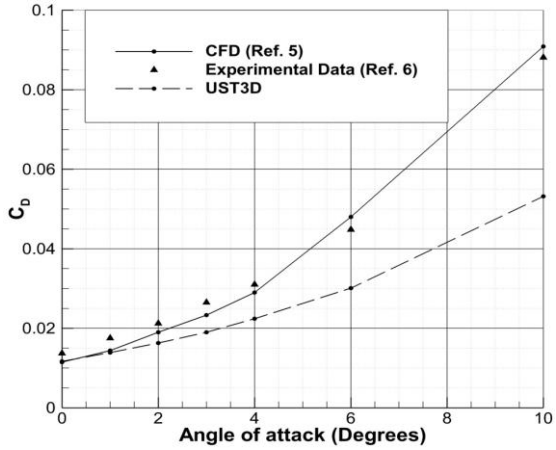

Figure 6. Drag coefficient values for different angles of attack at Mach 4.

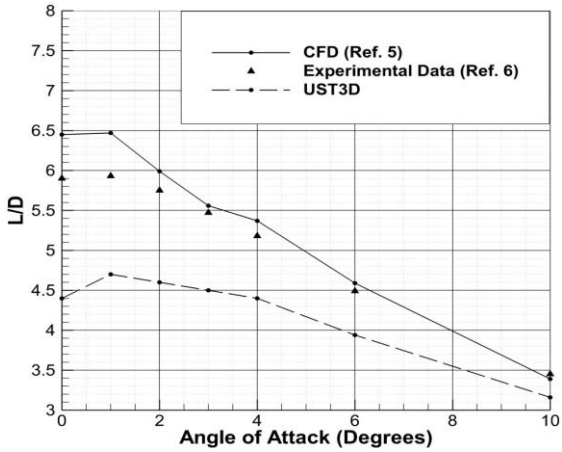

Figure 7. Lift-to-drag ratio values for different angles of attack at Mach 4.

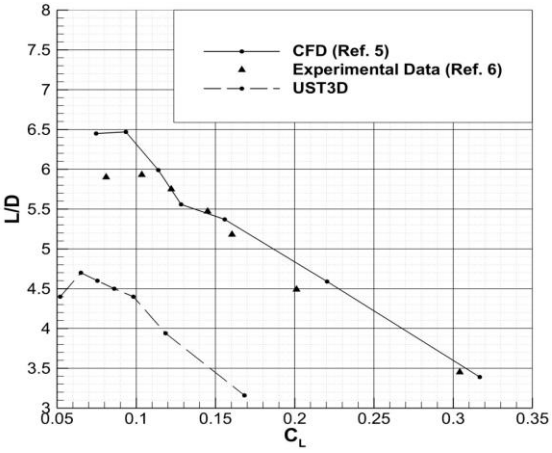

Figure 8. Lift-to-drag ratio as lift coefficient function at Mach 4.

The maximum lift-to-drag ratio occurs at 1° angle of attack. This parameter decreases as angle of attack increase. The aerodynamic performance degrades significantly at high angles of attack due to the drag coefficient increasing faster than lift coefficient growth. The acceptable agreement between the experimental values and UST3D code solutions occurs at high angles of attack.

6. Conclusions

The results obtained with the aid of the UST3D code showed that the aerodynamic parameters can be obtained with reasonable accuracy. It should be noted that the geometric model reproduction precision effects the numerical simulation success significantly. The difference in the definition of the reference area is another factor resulting in the error.

Acknowledgments
The work was performed within the framework of the Program of basic research of the Russian academy of sciences and was supported by the Russian Foundation for Basic Research grant No.16-01-00379. Author thanks Professor S.T. Surzhikov for the help.

References

[1] Maccoll J W 1937 The conical shock wave formed by cone moving at a high speed. *Proc. of the Royal Society of London. Series A, Containing Papers of a Mathematical and Physical Character* vol 159 pp 459–472
[2] Maxwell J R 2016 Hypersonic Waverider Stream Surface Actuation for Variable Design Point Operation *52nd AIAA/SAE/ASEE Joint Propulsion Conference July 25–27 Salt Lake City UT AIAA Paper 16–4706*
[3] Bowcutt K G, Anderson J D 1987 Viscous optimized hypersonic waveriders *AIAA 25th Aerospace Sciences Meeting January 12–15 Reno Nevada AIAA Paper 87–0272*
[4] Corda S, Anderson J D 1988 Viscous optimized hypersonic waveriders designed from axisymmetric flow fields *AIAA 26th Aerospace Sciences Meeting January 11–14 Reno Nevada AIAA Paper 88–0369*
[5] Cockrell Ch E 1993 Interpretation of waverider performance data using computational fluid dynamics *AIAA 24th Fluid Dynamics Conference July 6–9 Orlando FL AIAA Paper 93–2921*
[6] Bauer S X S, Covell P F, Forrest D K, McGrath B E 1990 Preliminary assessment of a Mach 4 and a Mach 6 waverider *Proc. of first international hypersonic waverider symp., University of Maryland, College Park MD* pp 1–24
[7] Zheleznyakova A L and Surzhikov S T 2013 Application of the Method of Splitting by Physical Processes for the Computation of a Hypersonic Flow over an Aircraft Model of Complex Configuration *High Temperature* **51** (6) pp 816–829
[8] Zheleznyakova A L and Surzhikov S T 2014 Calculation of a Hypersonic Flow over Bodies of Complex Configuration on Unstructured Tetrahedral Meshes Using the AUSM Scheme *High temperature* **52** (2) pp 274–284